Science Bulletin 64 (2019) 679–689

Contents lists available at ScienceDirect

Science Bulletin

journal homepage: www.elsevier.com/locate/scib

Article

Radial extracorporeal shock wave promotes the enhanced permeability and retention effect to reinforce cancer nanothermotherapeutics

Chunyang Yin [a,b], Shunhao Wang [a,b], Quanzhong Ren [a,b], Xinming Shen [a,b], Xiaodong Chen [c], Yajun Liu [d,*], Sijin Liu [a,b,*]

[a] *State Key Laboratory of Environmental Chemistry and Ecotoxicology, Research Center for Eco-Environmental Sciences, Chinese Academy of Sciences, Beijing 100085, China*
[b] *University of Chinese Academy of Sciences, Beijing 100049, China*
[c] *School of Aerospace Engineering, Beijing Institute of Technology, Beijing 100081, China*
[d] *Orthopedic Shock Wave Treatment Center, Department of Spine Surgery, Beijing Jishuitan Hospital, Beijing 100035, China*

ARTICLE INFO

Article history:
Received 15 March 2019
Received in revised form 7 April 2019
Accepted 8 April 2019
Available online 11 April 2019

Keywords:
Radial extracorporeal shock wave
Nanomedicine
Nanothermotherapeutics
Vasodilation
Tumor perfusion

ABSTRACT

Since most cancer nanomedicine relies on the enhanced permeability and retention (EPR) effect to eradicate tumors, strategies that are able to promote nanoparticle (NP) delivery and extravasation are presupposed to elevate the EPR effect for more effective cancer therapeutics. However, nanothermotherapeutics still suffers from limited drug delivery into tumor sites, for even though numerous efforts have been made to enhance the selective tumor targeting of NPs. In this study, we uncovered that radial extracorporeal shock wave therapy (rESWT), an important approach in physical therapy that has been overlooked in cancer treatment in the past, can largely improve the EPR-dependent tumor uptake of NPs. We here defined the optimal low dosage and desirable combinatory manner for rESWT in driving NP accumulation towards tumors. Two underlying biophysical mechanisms responsible for the rESWT-enhanced EPR effect were proposed. On one hand, rESWT-conducted compressive and tensile forces could relieve high intra-tumoral pressure; on the other hand, rESWT-induced cavitation bubbles could directly distend and disrupt tumor blood vessels. All these together synergistically promoted vessel vasodilation, tumor perfusion and NP extravasation. Further experiments revealed that the combinatory therapeutics between rESWT and nanothermotherapeutics greatly improved the tumor-killing efficacy. Thus, our findings open a new path to improve EPR-mediated drug delivery with the assistance of rESWT.

1. Introduction

Through making best use of the enhanced permeability and retention (EPR) effect, nanoparticles (NPs) could more readily localize in tumor tissues than in normal tissues [1–3]. The EPR effect is explained by abnormal vessels, in form and architecture, including the poorly organized alignment of endothelial cells and a deficiency of the smooth muscle layer [4]. Any exotic and endogenous factors that could promote the delivery and extravasation of NPs are believed to enhance the EPR effect in solid tumors [5–7]. Nonetheless, despite recent encouraging progresses, insufficient targeting and limited tumor localization impede the satisfactory efficacy of nano-drugs in cancer treatment [8]. Drug delivery towards tumors substantially relies on the perfusion efficiency of blood vessels, including capillaries. Meanwhile, growth-induced high intra-tumoral pressure otherwise compresses tumor vasculatures, leading to poor blood perfusion and blocked drug delivery [9–11]. To this end, even sophisticatedly designed NPs with active targeting ligands cannot be effectively delivered into tumors, with less than 0.0014% of the injected dose eventually reaching the targeted cancer cells [12]. Therefore, thus far, a myriad of approaches is being explored to favor the delivery and extravasation of nano-drugs from blood vessels into tumor microenvironment.

Radial extracorporeal shock wave therapy (rESWT) has long been exploited to treat inflammation-related disorders, musculoskeletal diseases, cardiac ischemia, and wound healing [13–17], while a rather limited understanding has been achieved in rESWT-related cancer therapeutics. In reality, the permeability of the tumor vasculature and regional blood flow are significant factors in governing the EPR effect [18]. rESWT has been demonstrated to expediate the gap formation within the blood vessel endothelial walls through which rESWT could expel the proinflammatory intermediates, including prostaglandin E2 (PGE2) and 5-hydroxytryptamine (5-HT), to ameliorate the inflammation symptoms [14,19]. Similar to ultrasound [20], tumor architecture

---

* Corresponding authors.
E-mail addresses: drliuyajun@163.com (Y. Liu), sjliu@rcees.ac.cn (S. Liu).

https://doi.org/10.1016/j.scib.2019.04.017
2095-9273/

may be altered to increase leakiness by rESWT-induced cavitation bubbles, and blood flow could also be remarkably boosted in response to rESWT [14]. Under this setting, rESWT-induced endothelial leakiness should supposedly favor the delivery and extravasation of nano-drugs into the tumor microenvironment and thereby reinforce tumor targeting and the following treatment. In fact, recent burgeoning evidence indicates that extracorporeal shock wave (ESW) is applicable to treat tumors, due to increased plasma membrane permeability and intracellular drug concentration that are ascribed to ESW-driven cavitation [21–23]. Thus, it would be of proven importance to extend ESW applications in cancer therapeutics, although a wider caliber of combinatory therapies and deeper understanding of molecular mechanisms are warranted.

The primary objective of the current study is to test the hypothesis that rESWT increases the EPR effect of nano-drugs for greater cancer nanotherapeutics. Our combined results demonstrated that rESWT robustly reinforces cancer nanothermotherapeutics by increasing NP extravasation. This study unearthed the great value of rESWT in combination with nanomedicine in cancer therapeutics.

2. Materials and methods

2.1. Materials

Cholesterol, dipalmi-toylphosphatidylcholine (DPPC) and polyethylene glycol (PEG) conjugated distearinphosphatidyl ethanolamine (DSPE-mPEG5k) were purchased from the J&K Scientific Ltd. and the Shanghai Ponsure Biotech Inc., respectively. 1,1′-Dioctadecyl-3,3,3′,3′-tetramethylindocarbocayanine perchlorate (DiI) and 1,1′-dioctadecyl-3,3,3′,3′-tetramethylindotricarbocyanine iodide (DiR) were obtained from the AAT Bioquest Inc. PEG-coated gold nanoparticles (AuNPs) and gold nanoshells (AuNSs) were purchased from nanoComposix company (San Diego, CA, USA). High pure nitric acid and hydrochloric acid were purchased from the Sinopharm Chemical Reagent Co. (Beijing, China). Ultrapure water was obtained from a Milli-Q Gradient system (SAS-67120, Millipore, Molsheim, France).

2.2. Liposome synthesis

To prepare DiR/DiI-liposome NPs following a standard method, as described previously [24]. Briefly, the mixed solutions of DPPC, cholesterol, DSPE-mPEG5k and DiR/DiI at a molar ratio of 6:4:0.5:0.25 was dissolved in 1 mL chloroform, and was then dried using a vacuum freeze-drying machinery. Next, the dried lipid film was hydrated with 1 mL phosphate buffered saline and stirred at 45 °C for 1 h, followed by extrusion through a 200 nm polycarbonate filter for 20 times and then a 100 nm polycarbonate filter for 20 times.

2.3. Characterization of NPs

The morphology of DiR/DiI-liposome NPs stained with 1.5% phosphotungstic acid was examined under a transmission electron microscopy (TEM, H-7500, Hitachi, Japan). AuNPs and AuNSs were visualized on a high-resolution TEM instrument (JEM-2100F, JEOL, Japan). The hydrodynamic diameter and zeta potential in deionized water were determined on a Zetasizer instrument (Malvern Nano series, Malvern, UK). Absorbance spectra of all NPs were recorded on a Shimadzu ultraviolet–visible–near-infrared (UV–vis–NIR) absorption spectrometer (UV-3600, Shimadzu Co., Japan).

2.4. Animal models and experimentation

Female BALB/c mice (6–8 weeks old, body weight weighing around 20 g) were purchased from the Vital River Laboratories (Beijing). All animal experimentation was approved by the Animal Ethics Committee at the Research Center for Eco-Environmental Sciences, Chinese Academy of Sciences. To establish the xenotransplanted tumor model, 2.0×10^5 CT26 cells were first suspended in 50 μL diluted Matrigel (Corning, USA), and were then subcutaneously injected into the right rear region on the back. Tumor volume was closely monitored using a caliper and calculated according to the formula used in related studies: $\text{volume} = \text{length} \times \text{width}^2/2$ [25–27]. When the tumor size reached 100–120 mm^3, the following treatments were launched.

2.5. In vivo fluorescent imaging of DiR-liposome

For *in vivo* fluorescent imaging of DiR-liposome NPs, 25 mice bearing comparable CT26 tumors were randomly divided into 5 groups: (1) the control group with DiR-liposome NP injection only; (2) and (4) groups with DiR-liposome NP injection 20 min prior to rESWT administration; (3) and (5) groups with DiR-liposome NP injection immediately after rESWT. To explore the optimal dosage, parameters for rESWT were set as follows, (i) 250 impulses with 1 bar and 1 Hz, equivalent to 0.04 mJ/mm^2 in 3 mm depth per second, referred to as $\text{rESWT}_{\text{low}}$; (ii) 500 impulses with 1 bar and 2 Hz, equivalent to 0.08 mJ/mm^2 in 3 mm depth per second, referred to as $\text{rESWT}_{\text{high}}$. After intravenous (i.v.) administration of 100 μL DiR-liposome NPs (at 1.25 mg/kg body weight) with or without different rESWT treatments, mice were anesthetized and imaged under a Xenogen IVIS spectrum (Caliper Life Sciences, USA) over the time course. The DiR fluorescence intensity was quantified using the average radiant efficiency ((photons/sec/cm^2/steradian)/(μW/cm^2)), as previously described [26].

For further quantitative analysis, mice were sacrificed at 24 h post treatment, the obtained tumors were weighed and homogenized in lysis buffer (containing 1% sodium dodecylsulfate (SDS), 1% Triton X-100, 10 mmol/L ethylenediaminetetraacetic acid (EDTA), 10 mmol/L dithiothreitol (DTT) and 40 mmol/L Tris acetate) with a tissue homogenizer. After centrifugation at 3000 r/min for 5 min, a multimode microplate spectrophotometer (Varioskan Flash, Thermo Fisher Scientific, US) was used to determine the fluorescence intensity of the clear homogeneous supernatants. To calculate the percentage of injection dose (ID%), the fluorescence intensity of DiR-liposome NPs was also measured.

2.6. Specimen digestion and Au mass determination

Au mass in each tumor specimen was quantified using an inductively coupled plasma mass spectrometer (ICP-MS, 8800 series, Agilent Technologies, Santa Clara, CA, USA). In brief, tumor samples were digested in a solution containing 400 μL of hydrochloric acid-nitric acid (3:1) at 75 °C overnight. And the digested solutions were diluted to 8 mL with the acid concentration below 5% (v:v), followed by ICP-MS analysis, as previously described [28].

2.7. Immunofluorescent staining

To visualize the tumor microvascular architecture, CD31 immunofluorescent staining was conducted according to an established protocol [24,29]. Immediately after treatment, fresh tumor tissues were imbedded in OCT compound, and then cut into 10 μm frozen slices. Afterwards, all slices were first incubated with rat-anti-mouse CD31 primary antibody (dilution 1:100, Biolegend Inc., CA, USA), and were then stained with a rhodamine conjugated goat-anti-rat secondary antibody (dilution 1:100, Proteintech Group Inc., USA). After counter-staining with 4,6-diamino-2-phenyl indole (DAPI), the fluorescent pictures were imaged on a confocal laser scanning microscopy (CLSM) instrument.

To characterize the diffusion of DiI-liposome NPs through tumor vessels after rESWT, mice bearing comparable CT26 tumors with or without rESWT were immediately i.v. injected with DiI-liposome NPs. Twenty-four hours later, all tumor samples were harvested and processed following the same method, as described above, where a goat-anti-rat secondary antibody conjugated with FITC was used instead (dilution 1:100, Proteintech Group Inc.). Quantitative analyses of blood vessel percentage, effective vascular area and positive red pixel region of DiI-liposome NPs were carried out with Image J software (NIH, Bethesda, MD, USA).

2.8. Tumor perfusion evaluation

To evaluate the blood flow of intra-tumoral microvasculature, the mice were placed on a power Doppler imaging equipment (Visualsonic Vevo® 2100 LAZER, Toronto, Canada) immediately after treatment. The instrument parameters were set as follows, frequency 32 MHz, Doppler gain 35.0 dB, depth 10.0 mm and width 14.0 mm.

2.9. In vivo combinatory nanothermotherapeutics with rESWT

Mice bearing comparable CT26 tumors were randomly divided into 6 groups: (I) control group; (II) rESWT group; (III) NIR group; (IV) rESWT + NIR group; (V) AuNSs + NIR group; (VI) rESWT + AuNSs + NIR group. rESWT (250 pulses, 0.04 mJ/mm^2 per pulse) was first conducted to group II, IV and VI. Immediately after rESWT, 100 μL of AuNSs (at 2 mg/kg body weight) were i.v. injected into group VI. Even without rESWT, the same mass of AuNSs were i.v. injected into group V. Twenty-four hours later, mice in group III, IV, V and VI were subjected to 808 nm laser irradiation with the power density of 1 mW/cm^2 for 5 min. Meanwhile, a thermal camera (FLIR Systems Inc., USA) was employed to record the real-time temperature and thermal images of the tumors. The same procedure was repeated twice on day 2 and day 4. The tumor volumes were recorded every other day, And the body weight changes were also monitored.

2.10. Statistical analysis

Experimental data were represented as mean ± standard derivation (SD). Independent t-test or one-way ANOVA test was carried out to determine the statistical significance. The statistical significance was set with $^*P < 0.05$ and $^\#P < 0.001$.

3. Results

3.1. Identifying optimal rESWT therapeutics in driving the tumor uptake of NPs

To probe the possibility of rESWT in promoting the EPR effect in cancer therapeutics, we first endeavored to figure out the optimal strategies, including dosage and combinatory manner, using a model material: DiR-labeled liposome NPs, which bear strong *in vivo* fluorescence [25,26,30]. We synthesized uniform, sphere-like liposome NPs with similar diameters of approximately 100 nm, as characterized by TEM analysis (Fig. 1a). The UV–vis–NIR absorption spectrum of DiR-liposome NPs revealed a characteristic peak around 755 nm, consistent with that of DiR (Fig. 1b). Dynamic light scattering (DLS) showed that the average hydrodynamic diameter of the DiR-liposome NPs was approximately 106 nm, and these NPs were negatively charged (Table S1 online). Next, we looked for the desirable dosage of rESWT in improving the EPR effect. Since ESW at high intensity would likely cause damage to tumors and surrounding tissues [21,31,32], two dosages with relatively low energy flow density (EFD) were thereby chosen based on our previous study [33], 0.04 mJ/mm^2 (here, referred to as rESWT$_{\text{low}}$) and 0.08 mJ/mm^2 (here, referred to as rESWT$_{\text{high}}$) specifically. Furthermore, to determine the preferential manner of rESWT in combination with NPs, two models were conducted, i.e., model 1 with an i.v. injection of DiR-liposome NPs through tail vein 20 min before rESWT, and model 2 with an i.v. injection of DiR-liposome NPs immediately after rESWT (Fig. 1c). To address these questions, we established a xenotransplantation mouse model of colon cancer cells with similar tumor size in all groups prior to treatment, as delineated in Fig. 1c. Fig. 1d–f showed an overall trend of enhanced uptake of DiR-liposome NPs upon rESWT compared to the group without rESWT. Regarding the dosage, the higher dose at 0.08 mJ/mm^2 did not improve NP uptake into tumors compared with the lower dose at 0.04 mJ/mm^2, even with a modest increase (Fig. 1d–f). With respect to the combinatory mode of rESWT, overall, model 2 overall appeared better in gathering DiR-liposome NPs than the model 1 over time (Fig. 1d–f, $P < 0.05$). Twenty-four hours after the administration of DiR-liposome NPs, tumors were ablated and lysed for DiR fluorescence determination, and quantitative data showed the greatest DiR fluorescence in mice upon rESWT at 0.04 mJ/mm^2 under the mode of rESTW with immediate liposome NP injection, with a 30%–60% increase relative to the other 3 rESWT-treated groups (Fig. 1f, $P < 0.05$). These data together indicated that the manner of rESWT followed by immediate NP injection would be more efficient in driving NP localization into tumors, and an EFD at 0.04 mJ/mm^2 manifested greater efficacy in enhancing the EPR effect than the EFD at 0.08 mJ/mm^2. To this end, we selected model 2, namely NP administration immediately after rESWT, and used the EFD at 0.04 mJ/mm^2 in the following experiments.

3.2. Enhanced NP targeting inside tumors with the aid of rESWT

To substantiate the reinforced intra-tumoral accumulation of liposome NPs upon rESWT, we further tracked the NP distribution inside tumors. To realize the in situ intra-tumoral characterization of NPs, the CLSM was used to sufficiently visualize the NPs. Since DiR dye is a NIR fluorescent dye that cannot be visualized using CLSM [30], DiI was then replaced to label liposome NPs in order for adequate in situ fluorescent imaging under CLSM. As shown in Fig. 2a, we synthesized liposome NPs labelled with DiI dye, showing an average size of approximately 100 nm similar to that of DiR-liposome NPs. Analogously, DiI-liposome NPs were negatively charged in water with an average hydrodynamic diameter of approximately 142 nm (Table S1 online). The UV–vis-NIR absorption spectrum displayed a characteristic peak at 550 nm for the DiI-liposome NPs, indicating a shift to the right compared with DiI itself (Fig. 2b). Following the established rESWT strategy, as described above, DiI-liposome NPs were i.v. administrated immediately post rESWT (Fig. S2 online). Thereafter, tumors were collected for frozen sections 24 h after NP injection. As shown in Fig. 2c, the fluorescent images revealed stronger DiI fluorescence (in red) in tumor sections with rESWT relative to that in tumors without rESWT, and quantified data defined >2-fold increase (Fig. 2d, $P < 0.05$). Moreover, CD31, a surrogate of vascular endothelium [34], was stained to localize tumor vasculatures (Fig. 2c, in green). As shown in Fig. 2c, most DiI signals were co-localized to the sites with CD31 signals (pointed at by white arrows) in tumors from the control group, in parallel to the limited extravasation capability out of blood vessels for NPs with a diameter of approximately 100 nm [35]. However, DiI fluorescence was found to diffuse away from CD31 fluorescence responding to

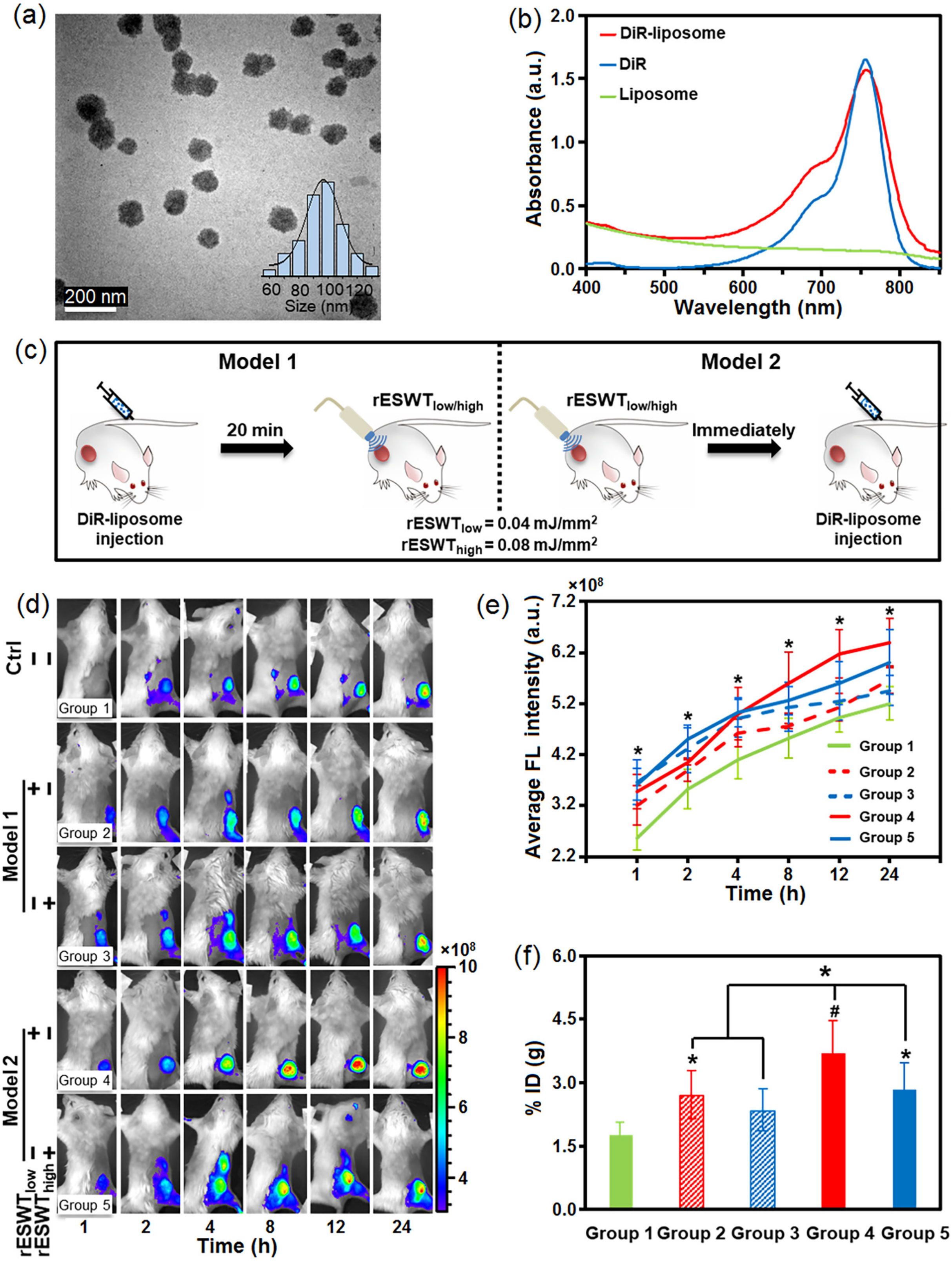

Fig. 1. Characterization of the optimal rESWT therapeutic strategies. (a, b) A TEM image and UV–vis-NIR absorption spectrum of DiR-liposome NPs. The inset panel in (a): the diameter distribution of DiR-liposome NPs. (c) Schematic illustration in defining the optimal conditions for rESWT to enhance tumor accumulation of NPs. (d) The *in vivo* NIR fluorescent imaging of mice over time in different groups ($n = 5$). (e) Quantitative data of the average DiR fluorescence (FL) intensities in tumors for different groups in (d) ($n = 5$). Asterisk (*) indicates $P < 0.05$ for Groups 4 and 5 compared to Group 1. (f) Quantified data for DiR-liposome NP accumulation in dissected tumors, as reflected by the DiR fluorescence at 24 h in (d) ($n = 5$). Data are shown as % of injection dose (ID) per g tumor samples. Asterisks (*) for Group 2 and Group 5 indicate $P < 0.05$ and pound sign (#) for Group 4 indicates $P < 0.001$, compared to Group 1. Here, independent *t-test* was used for comparison between two groups.

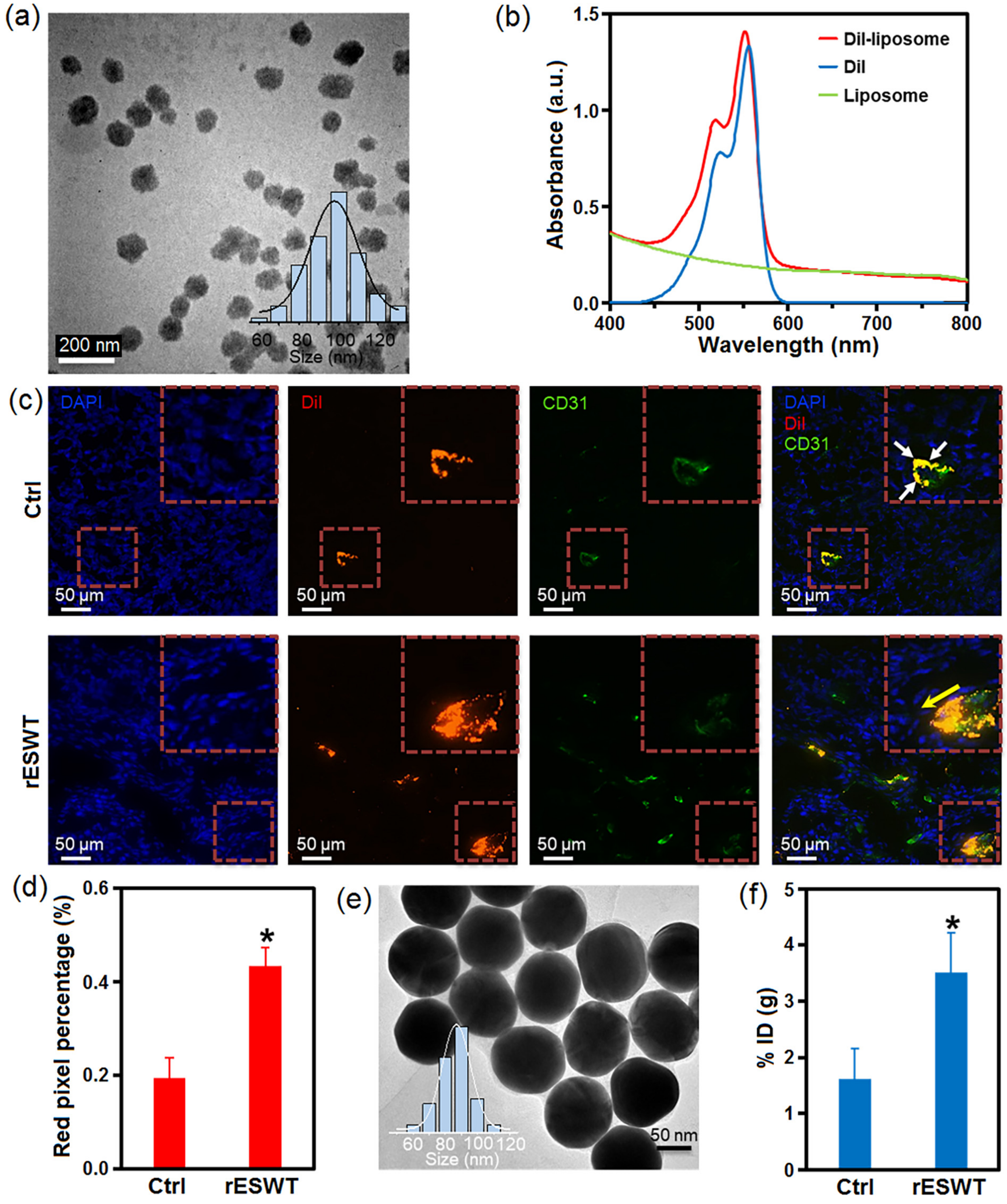

Fig. 2. Enhanced NP targeting into tumors with the aid of rESWT. (a, b) A TEM image and UV–vis–NIR absorption spectrum of DiI-liposome NPs. The inset panel in (a): the diameter distribution of DiI-liposome NPs. (c) Immunofluorescent staining images of tumor slices at 24 h post rESWT administration. (d) Quantitative analysis of the percentage of positive red pixel region using the Image J software based on 8 different graphs for each group. (e) A TEM image of AuNPs. The inset panel in (e): the diameter distribution of AuNPs. (f) Au content in tumors from the control and rESWT-treated mice at 24 h post administration ($n = 5$). Data are shown as % of injection dose (ID) per g tumor. Asterisk (*) indicates $P < 0.05$, compared to the control group.

rESWT (denoted by the yellow arrow, Fig. 2c). These observations therefore suggested that rESWT expediated the extravasation of these NPs from blood vessels into the tumor interstitial space.

To further corroborate this finding, we deliberately employed a different type of NPs: PEG-coated AuNPs in spherical morphology with the average diameter of approximately 100 nm, as characterized by the TEM analysis (Fig. 2e). In analogy to the liposome NPs, the average hydrodynamic diameter of AuNPs was approximately 130 nm, and AuNPs were also negatively charged in water (Table S1 online). Using the same mouse model for the DiI-liposome NPs, more than 2-fold increase of AuNP uptake by tumors was demonstrated in tumors upon rESWT compared with that in those tumors without rESWT, as evidenced by the ICP-MS detection of Au mass (Fig. 2f, $P < 0.05$). Collectively, these results uncovered that rESWT facilitated NP extravasation and localization into the tumor microenvironment through enhancing the EPR effect.

3.3. rESWT provoked endothelial vasodilation of tumor vasculature to promote tumor perfusion

Next, in an effort to exploit the underlying mechanisms responsible for the rESWT-mediated elevation of the EPR effect, more detailed examination was carried out. To depict the changes in tumor vasculatures, different regions of the tumors, namely from the exterior site to the middle and interior sites, were closely scrutinized using the rhodamine-conjugated CD31 antibody. As delineated in Fig. 3a, blood vessels in the exterior, middle and interior regions of the tumors were stained in red, and the fluorescent intensity was much greater (approximately 2 times) across all

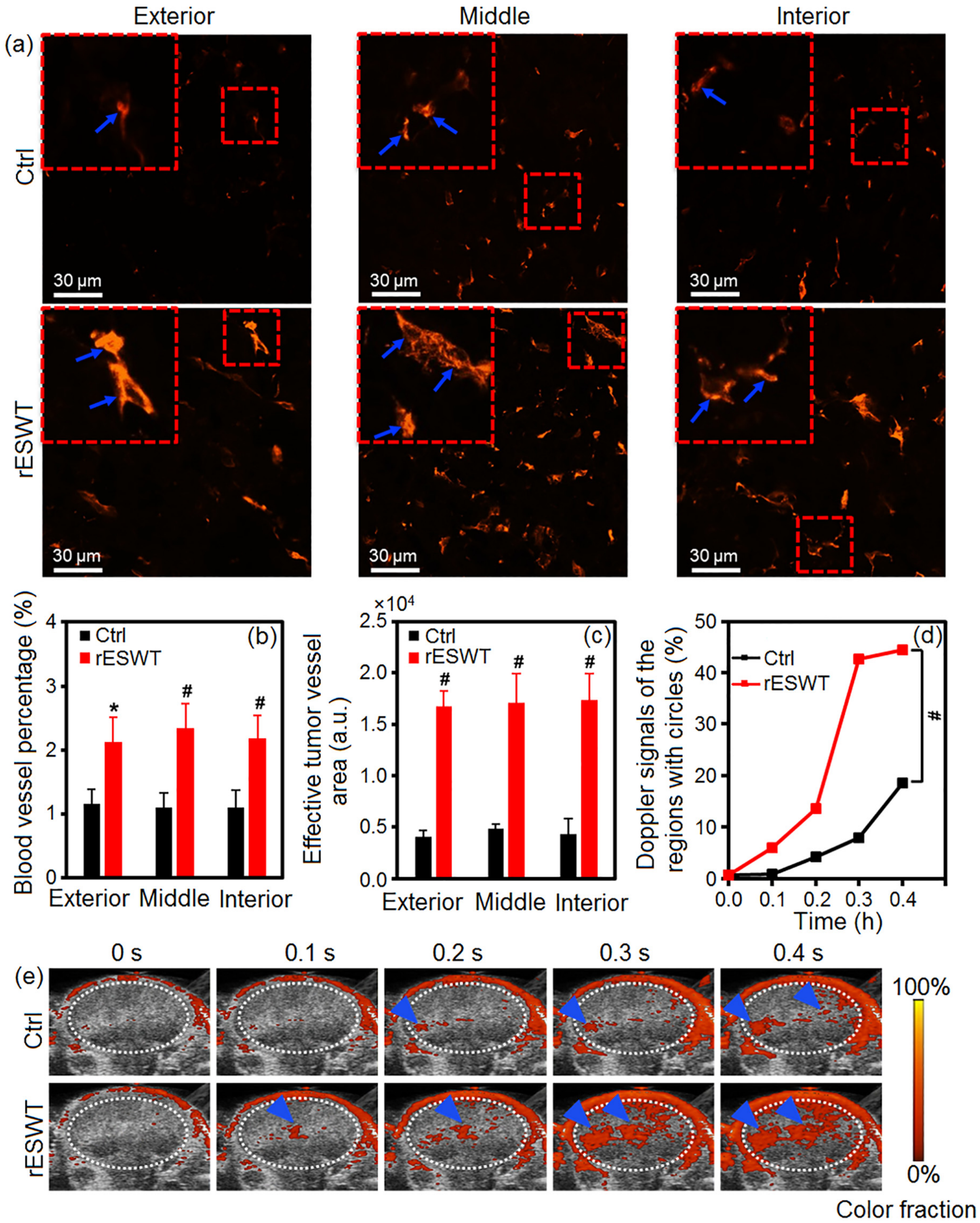

Fig. 3. rESWT induced endothelial vasodilation of tumor vasculature. (a) Representative immunofluorescent images of tumor blood vessels from exterior, middle and interior regions for tumors with or without rESWT ($n = 5$). Tumor vasculatures stained with anti-CD31 antibody are shown in red. Quantitative analysis of (b) blood vessel percentage and (c) effective vascular area in (a) using the Image J software. Asterisk (*) indicates $P < 0.05$ and pound sign (#) indicates $P < 0.001$, compared to the control group. (d) Power Doppler imaging analysis of the above mice with or without rESWT. White dashed circles denote intra-tumoral regions and blue arrows indicate Doppler signals. (e) Quantitative data are shown in (d) ($n = 3$). The P value was calculated by one-way ANOVA test.

regions in tumors treated by rESWT than that in tumors without rESWT, with quantified data shown in Fig. 3b ($P < 0.05$). Furthermore, the number of dilated blood vessels, as denoted by blue arrows in Fig. 3a, was also significantly increased in the rESWT-treated group, as characterized by an approximately 4-fold increase of the effective area compared to that in the control group (Fig. 3a and c, $P < 0.001$). These observations suggested that rESWT induced significant angiectasis in tumors, resulting in facilitated blood flow into tumor interstitial space. Under this context, we thus evaluated tumor perfusion with power Doppler imaging, an established method for superb tumor microvasculature imaging and the determination of blood volume and velocity [36]. As shown in Fig. 3d, Doppler signals emerged mainly in the surrounding regions with the maximum of 18.5% prior to rESWT, and fairly strong Doppler signals dispersed nearly throughout the whole of the tumors after rESWT over time with a maximum of 44.5%. Fig. 3e indicates a rather large difference in tumor perfusion of the white dashed circled regions ($P < 0.001$). These findings therefore unveiled that rESWT indeed significantly enhanced the passage of the blood stream into tumors and, in other words, reinforced tumor perfusion.

In fact, most solid tumors possess a more abundant vascular network compared to normal tissues [24,37]. However, tumor structural components (e.g., compact cells in tumor microenvironment and extracellular matrix) exert high intra-tumoral pressure on tumor vasculatures, especially capillaries, leading to a compressed morphology of endothelial cells and disordered perfusion state of the vasculatures [9–11]. Therefore, solid tumor constituents are the main depleting targets for pharmacological strategies to improve drug delivery [10,38], and emerging studies have focused on depleting extracellular matrix to improve NPs delivery [39,40]. Likewise, compressive and tensile forces triggered by rESWT inevitably cause microinjury and depletion on tumor constituents of the localized area, which should supposedly alleviate high intra-tumoral pressure, hence decompressing tumor vasculatures, as reflected by our experimental evidence of increased blood vessel density and effective vascular area (Fig. 4a).

3.4. rESWT-generated cavitation likely mediated blood vessel permeability

Cavitation refers to rapid changes of pressure in a solution, coupled to the formation of small vapor-filled cavities, also named bubbles, and these cavities will collapse upon high pressure [41]. It has been demonstrated that ultrasound-induced cavitation plays a crucial rule in permeabilizing blood vessels and facilitating drug delivery [42]. rESWT can create cavitation bubbles inside water [43], but whether cavitation bubbles could be generated inside blood is still a mystery, partly due to the limitations of current *in vitro* and *in vivo* models. To understand the role of rESWT-induced cavitation effects in promoting endothelial permeability of tumor vasculature, we carried out high-speed imaging analyses for rESWT-generated bubbles to model blood with serum, the transparent nature of which allowed for the direct visualization of cavitation bubbles. Fig. 4b shows the dynamics of a bubble cloud inside serum. It took approximately 147 μs from generation until the collapse of the bubbles, and the size of bubbles expanded to a maximum volume of approximately 0.24 mm at 88.2 μs (Fig. 4b and Supplementary Movie online). These generated bubbles at a size range are subjected to direct interaction with tumor blood vessels during their volumetric oscillations, similar to ultrasound or laser induced cavitation effects [44–47]. Under this setting, blood vessels could be vasodilated when bubbles grew to their maximum volume, and endothelia cells could be injured during volumetric oscillations. As a result, these changes gave rise to dilated blood vessels and increased endothelial leakiness that would facilitate NP extravasation, as delineated in Fig. 4a, similar to a recent study [48]. Collectively, both rESWT-triggered mechanical forces and cavitation effects synergistically contributed to boosting blood perfusion in the tumor microenvironment and endothelial leakiness of the tumor vasculature, yielding a beneficial condition for NP-mediated drug delivery.

3.5. rESWT considerably magnified the efficacy of nanothermotherapeutics

The above findings opened a new path to improve EPR-mediated drug delivery with the assistance of rESWT, and thus encouraged us to explore the likelihood of combinatory therapeutics between rESWT and nanothermotherapeutics. To realize this goal, we intentionally used AuNSs that harbor pronounced thermotherapeutic properties. Fig. 5a manifests typical nanoshell morphology with an average size of approximately 100 nm, with the maximum absorption wavelength remaining around 808 nm (Fig. 5b). Based on the DLS measurement, the average hydrodynamic diameter of AuNSs was approximately 132 nm with negative charge in water (Table S1 online). Afterwards, the thermotherapeutic efficacy of AuNSs at low dosage was assessed both with and without assistance of rESWT in the mouse model bearing CT26 tumors. Based on the previous experimental setup, 24 h after the administration of AuNSs +/− rESWT, mice were anesthetized and subjected to irradiation under an 808 nm laser at 1.0 W/cm^2 for 5 min (Fig. S2 online). To track the real-time temperature changes of tumors, an infrared thermal camera was used during the irradiation by focusing the spot laser beam onto the whole tumor regions, as indicated by dashed circles in Fig. 5c. Thermal imaging pictures displayed a marked increase of irradiation-induced temperature at the xenotransplanted tumor sites over time after the administration of AuNSs, and a greater extent of temperature increase was observed in tumors upon AuNSs together with rESWT, as evidenced in Fig. 5c. Quantified data showed more than 2-fold increase of temperature in tumors upon AuNSs with rESWT compared to that upon AuNSs only (Fig. 5d, $P < 0.001$). Also, the maximum temperature in the tumors upon AuNSs with rESWT reached 47 °C, which is enough to kill solid tumor cells [28,49]. These results hence signified the outstanding thermotherapeutic efficacy of AuNSs with the assistance of rESWT.

Next, the tumor-killing efficacy was determined after different treatments, as described in Fig. 5e. The tumor sizes and body weights were monitored every other day for 14 d. The body weight recording did not find significant alterations for these mice responding to these treatments (Fig. S3 online), indicating sufficient biosafety and bio-compatibility of these treatments. Additionally, no overt toxicity (including no abnormal activities and diet) were observed in those mice with different treatments. During the treatment period, tumor growth was greatly suppressed in the AuNSs + NIR group, showing no significant increase of the tumor volume on day 8 post-administration, compared to the control group and other groups ($P < 0.001$); however, the tumors were nearly completely ablated in the rESWT + AuNSs + NIR group after 4 days of treatment (Fig. 4e, $P < 0.001$). The final tumor images confirmed these huge differences among these treatments (Fig. 5f). Together, these data suggested the greatly improved thermotherapeutic efficacy of AuNSs in eliminating tumors with the assistance of rESWT, highlighting the rationale of this synergistic therapeutics.

4. Discussion and conclusions

Relative to other physical therapeutic approaches, such as magnetic field-guided NP tumor targeting and ultrasound-mediated enrichment of NPs towards tumors [50,51], rather limited studies

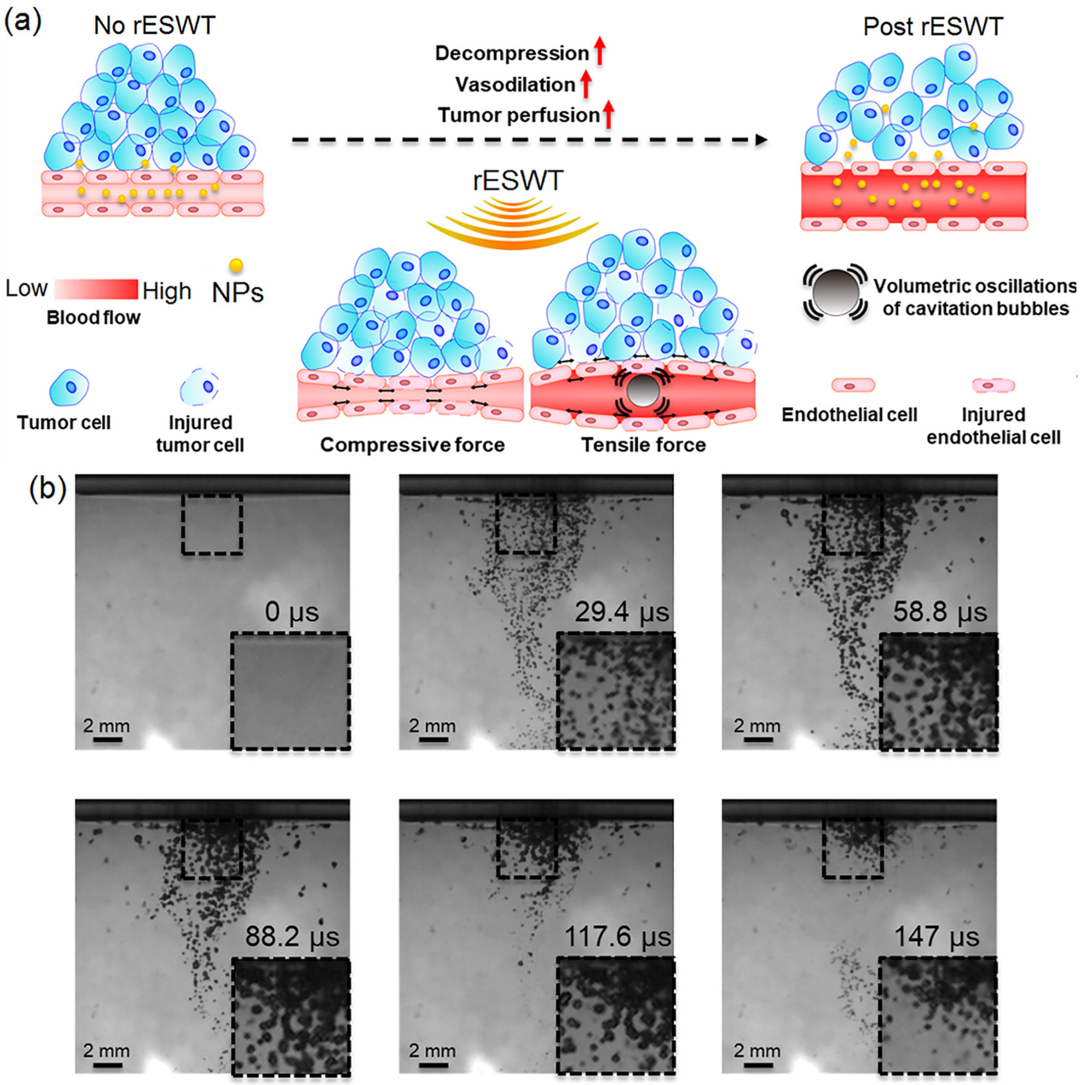

Fig. 4. rESWT alleviated intra-tumoral pressure and increased blood vessel permeability. (a) A working model showing the mechanism underlying rESWT-induced changes to vasculatures and tumor microenvironment. (b) Cavitation bubble dynamics captured by high-speed camera after one impulse of rESWT with 1 bar and 1 Hz in serum.

have combined ESW with nanomedicine as anticancer therapy thus far. Only a few studies employed ESW as a trigger for drug release [52,53] or sonodynamic therapy [54,55], whereas no studies have assessed the potential influence of rESWT on the EPR effect. In the current study, we uncovered the combinatory therapeutics between rESWT and nanothermotherapeutics in elevating the tumor-killing efficacy through enhanced EPR effect. With respect to the underlying mechanisms, our results deciphered that both mechanical forces and cavitation bubbles induced by rESWT accounted for the enhanced EPR effect. On one hand, compressive and tensile forces could relieve intra-tumoral pressure, resulting in elevated tumor perfusion. On the other hand, rESWT-induced cavitation bubbles could directly distend tumor blood vessels, coupled to an increased leakiness. In fact, rESWT-induced cavitation bubbles mainly took effect in liquid [56], namely blood, whereas rESWT-conducted mechanical forces predominantly in soft tissues [57]. Hence, both mechanisms should differentially but synergistically account for the elevated EPR effect induced by rESWT.

In contrast to this work, previous studies only looked at ultrasonic sonoporation caused by cavitation [5]. Of note, rESWT has no heating effects [23], making a desirable feature for clinical use. These features together endow rESWT a safer and more convenient clinical therapy than ultrasound from the perspective of combinatory nanomedicine in cancer treatment. Impaired perfusion is closely associated with reduced oxygen supply, causing a hypoxic tumor microenvironment that applies for tumor resistance of radiotherapy (RT) and photodynamic therapy (PDT) [10,24,29]. Meanwhile, hypoxia would recruit tumor-associated macrophages (TAMs) for polarization into an immunosuppressive type, namely M2 subtype, generating tumor progression and an immunosuppressive tumor microenvironment [24]. Our data unveiled the improved tumor perfusion with assistance of rESWT, providing the rationale in combination with RT, PDT and immunotherapy in the future. Nevertheless, more efforts should be invested to address existing knowledge gaps, including *in vivo* cavitation effects induced by rESWT.

To summarize, this study unveiled the encouraging usage of rESWT in enhancing the EPR effect to reinforce cancer nanothermotherapeutics. Our results add to the promising applications of rESWT in cancer therapeutics, and rESWT-assisted EPR effect for NP tumor targeting could be taken into consideration for nanomedicine to treat cancer.

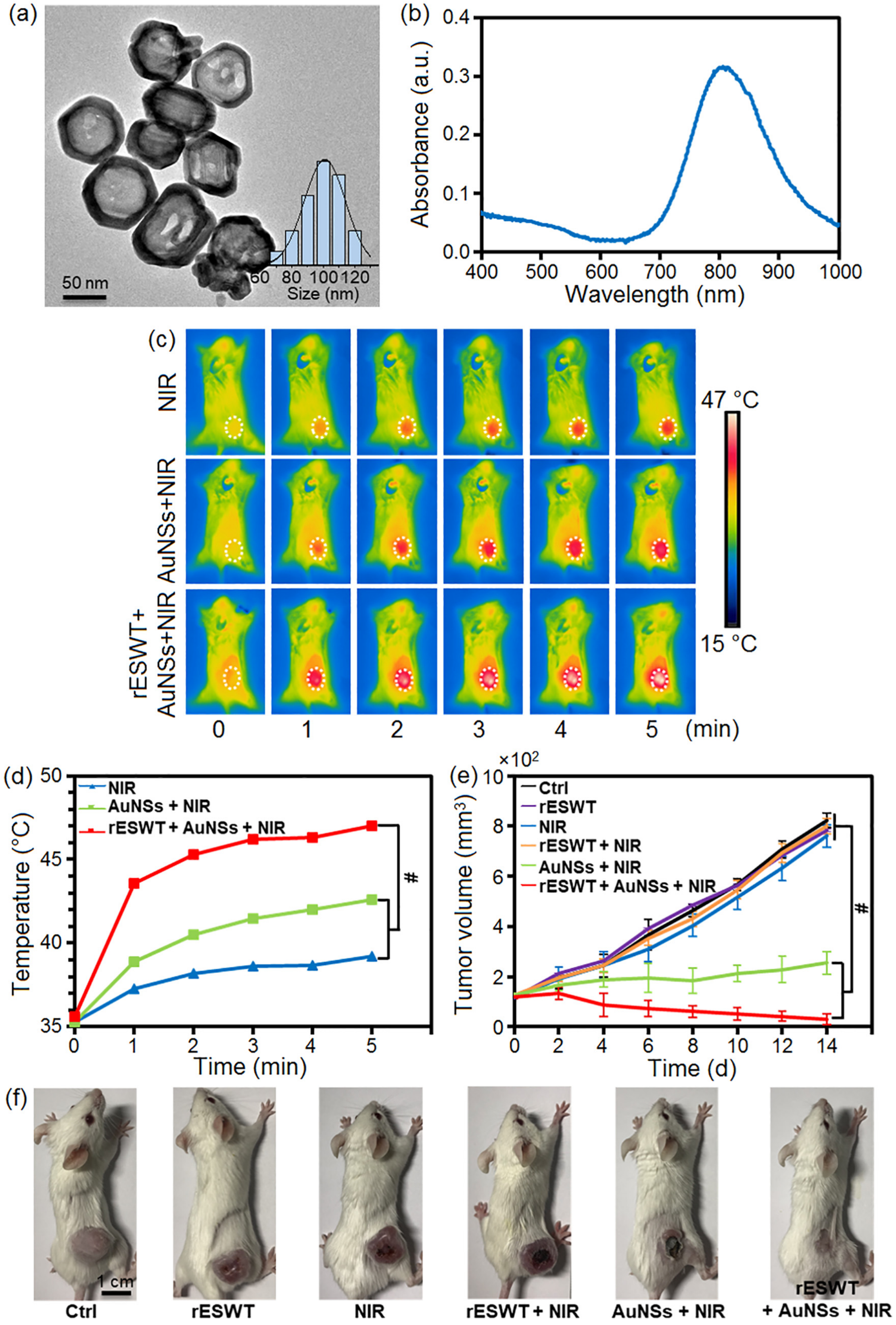

Fig. 5. rESWT magnified the efficacy of nanothermotherapeutics. (a, b) A TEM image and UV–vis-NIR absorption spectrum of AuNSs. The inset panel in (a): the diameter distribution of AuNSs. (c) Time-lapsed *in vivo* infrared thermal imaging in different groups with an infrared thermal camera. White dashed circles denote the tumor areas in mice. (d) Quantified data showing the corresponding tumor temperature change in (c). The *P* value was calculated by one-way ANOVA test. (e) Tumor growth curves of different groups upon diverse treatments ($n = 5$). Control group: saline injection only; rESWT group: rESWT administration; NIR group: NIR irradiation; rESWT + NIR group: NIR irradiation 24 h post rESWT; AuNSs + NIR group: NIR irradiation 24 h post AuNSs injection; rESWT + AuNSs + NIR group: NIR irradiation 24 h post combinatory therapeutics between rESWT and AuNSs. One-way ANOVA test was used to determine statistical significance among groups. (f) The final representative photographs captured on day 14 post-treatment.

Conflict of interest

The authors declare that they have no conflict of interest.

Acknowledgments

This work was supported by the National Natural Science Foundation of China (21425731, 21637004, 11772343, and 11402274), the Beijing Natural Science Foundation (8191002), Beijing Institute of Technology Research Fund Program for Young Scholars, Beijing Nova Programme Interdisciplinary Cooperation Project and the Strategic Priority Research Program of the Chinese Academy of Sciences (XDB14000000).

Author contributions

Yajun Liu and Sijin Liu conceived and designed the study. Chunyang Yin, Shunhao Wang, Quanzhong Ren, Xinming Shen and Xiaodong Chen carried out the experiments and analyzed the data. Sijin Liu, Yajun Liu, Xiaodong Chen and Chunyang Yin wrote and revised the manuscript.

Appendix A. Supplementary material

Supplementary data to this article can be found online at https://doi.org/10.1016/j.scib.2019.04.017.

References

[1] Golombek SKMJ, Theek B, Appold L, et al. Tumor targeting via EPR: strategies to enhance patient responses. Adv Drug Deliv Rev 2018;130:17–38.

[2] Lang TDX, Zheng Z, Liu Y, et al. Tumor microenvironment-responsive docetaxel-loaded micelle combats metastatic breast cancer. Sci Bull 2019;64:91–100.

[3] Deng L, Sun C, Yun B, et al. Functionalization of small black phosphorus nanoparticles for targeted imaging and photothermal therapy of cancer. Sci Bull 2018;63:917–24.

[4] Ac D. Tumor endothelial cells. Cold Spring Harb Perspect Med 2012;2:a006536.

[5] Ojha TPV, Shi Y, Hennink WE, et al. Pharmacological and physical vessel modulation strategies to improve epr-mediated drug targeting to tumors. Adv Drug Deliv Rev 2017;15:44–60.

[6] Shi JKP, Wooster R, Farokhzad OC. Cancer nanomedicine: progress, challenges and opportunities. Nat Rev Cancer 2017;17:20–37.

[7] Blanco ESH, Ferrari M. Principles of nanoparticle design for overcoming biological barriers to drug delivery. Nat Biotechnol 2015;33:941–51.

[8] Wilhelm STA, Dai Q, Ohta S, et al. Analysis of nanoparticle delivery to tumours. Nat Rev Mater 2016;1:16014.

[9] Chauhan VPMJ, Liu H, Lacorre DA, et al. Angiotensin inhibition enhances drug delivery and potentiates chemotherapy by decompressing tumour blood vessels. Nat Commun 2013;4:2516.

[10] Stylianopoulos TJR. Combining two strategies to improve perfusion and drug delivery in solid tumors. Proc Natl Acad Sci USA 2013;110:18632–7.

[11] Stylianopoulos TMJ, Chauhan VP, Jain SR, et al. Causes, consequences, and remedies for growth-induced solid stress in murine and human tumors. Proc Natl Acad Sci USA 2012;109:15101–8.

[12] Dai QWS, Ding D, Syed AM, et al. Quantifying the ligand-coated nanoparticle delivery to cancer cells in solid tumors. ACS Nano 2018;12:8423–35.

[13] Cj W. Extracorporeal shockwave therapy in musculoskeletal disorders. J Orthop Surg Res 2012;7:11.

[14] Mariotto SdPA, Cavalieri E, Amelio E, et al. Extracorporeal shock wave therapy in inflammatory diseases: molecular mechanism that triggers anti-inflammatory action. Curr Med Chem 2009;16:2366–72.

[15] Schmitz CCN, Milz S, Schieker M, et al. Efficacy and safety of extracorporeal shock wave therapy for orthopedic conditions: a systematic review on studies listed in the pedro database. Br Med Bull 2015;116:115–38.

[16] Yip HKLF, Chen KH, Sung PH, et al. Preclinical and clinical application of extracorporeal shockwave for ischemic cardiovascular disease. Transl Res Biomed Basel, Karger 2018;6:87–101.

[17] Zhang LFX, Chen S, Zhao ZB, et al. Efficacy and safety of extracorporeal shock wave therapy for acute and chronic soft tissue wounds: a systematic review and meta-analysis. Int Wound J 2018;15:590–9.

[18] Kobayashi HWR, Choyke PL. Improving conventional enhanced permeability and retention (epr) effects; what is the appropriate target? Theranostics 2013;4:81–9.

[19] Romeo PLV, Pagani D, Sansone V. Extracorporeal shock wave therapy in musculoskeletal disorders: a review. Med Princ Pract 2014;23:7–13.

[20] Sirsi SRBM. State-of-the-art materials for ultrasound-triggered drug delivery. Adv Drug Deliv Rev 2014;72:3–14.

[21] Frairia RBL, Catalano MG. Extracorporeal shock waves: perspectives in malignant tumor treatment. J Biol Regul Homeost Agents 2016;30:641–8.

[22] López-Marín LM, Millán-Chiu BE, Castaño-González K, et al. Shock wave-induced damage and poration in eukaryotic cell membranes. J Membrane Biol 2017;250:41–52.

[23] López-Marín LMRA, Fernández F, Loske A. Shock wave-induced permeabilization of mammalian cells. Phys Life Rev 2018;26–27:1–38.

[24] Chen QXL, Chen J, Yang Z, et al. Tumor vasculature normalization by orally fed erlotinib to modulate the tumor microenvironment for enhanced cancer nanomedicine and immunotherapy. Biomaterials 2017;148:69–80.

[25] Feng LCL, Dong Z, Tao D, et al. Theranostic liposomes with hypoxia-activated prodrug to effectively destruct hypoxic tumors post-photodynamic therapy. ACS Nano 2017;11:927–37.

[26] Feng LTD, Dong Z, Chen Q, et al. Near-infrared light activation of quenched liposomal ce6 for synergistic cancer phototherapy with effective skin protection. Biomaterials 2017;127:13–24.

[27] Guo M, Liu Z, Liu J, et al. Direct site-specific treatment of skin cancer using doxorubicin-loaded nanofibrous membranes. Sci Bull 2018;63:92–100.

[28] Gao JS-PM, Huang H, et al. Synthesis of different-sized gold nanostars for Raman bioimaging and photothermal therapy in cancer nanotheranostics. Sci China Chem 2017;60:1219–29.

[29] Song XFL, Liang C, Yang K, et al. Ultrasound triggered tumor oxygenation with oxygen-shuttle nanoperfluorocarbon to overcome hypoxia-associated resistance in cancer therapies. Nano Lett 2016;16:6145–53.

[30] Zhang RFL, Dong Z, Wang L, et al. Glucose & oxygen exhausting liposomes for combined cancer starvation and hypoxia-activated therapy. Biomaterials 2018;162:123–31.

[31] Lukes PZJ, Horak V, Hoffer P, et al. In vivo effects of focused shock waves on tumor tissue visualized by fluorescence staining techniques. Bioelectrochemistry 2015;103:103–10.

[32] Wörle KSP, Hofstädter F. The combined effects of high-energy shock waves and cytostatic drugs or cytokines on human bladder cancer cells. Br J Cancer 1994;69:58–65.

[33] Liu YCX, Guo A, Liu S, Hu G. Quantitative assessments of mechanical responses upon radial extracorporeal shock wave therapy. Adv Sci 2017;5:1700797.

[34] Chang YS, McDonald DM, Jones R, et al. Mosaic blood vessels in tumors: frequency of cancer cells in contact with flowing blood. Proc Natl Acad Sci USA 2000;97:14608–13.

[35] Cabral HMY, Mizuno K, Chen Q, et al. Accumulation of sub-100 nm polymeric micelles in poorly permeable tumours depends on size. Nat Nanotechnol 2011;6:815–23.

[36] Yokota K, Akiyama Y, Mimura T. Detection of synovial inflammation in rheumatic diseases using superb microvascular imaging: comparison with conventional power doppler imaging. Mod Rheumatol 2018;28:327–33.

[37] Gong H, Xiang J, Han X, et al. Hyaluronidase to enhance nanoparticle-based photodynamic tumor therapy. Nano Lett 2016;16:2512–21.

[38] Dolor ASFJ. Digesting a path forward: the utility of collagenase tumor treatment for improved drug delivery. Mol Pharm 2018;15:2069–83.

[39] Wang JY, Lu X, He X. Nanoparticle systems reduce systemic toxicity in cancer treatment. Nanomedicine 2016;11:103–6.

[40] Zhou H, Deng J, Lemons PK, et al. Hyaluronidase embedded in nanocarrier peg shell for enhanced tumor penetration and highly efficient antitumor efficacy. Nano Lett 2016;16:3268–77.

[41] Coussios CC. Applications of acoustics and cavitation to noninvasive therapy and drug delivery. Annu Rev Fluid Mech 2008;40:395–420.

[42] Dasgupta ALM, Ojha T, Storm G, et al. Ultrasound-mediated drug delivery to the brain: principles, progress and prospects. Drug Discov Today Technol 2016;20:41–8.

[43] Császár NB, Milz S, Sprecher CM, et al. Radial shock wave devices generate cavitation. PLoS One 2015;10:0140541.

[44] Caskey CF, Qin S, Dayton PA, et al. Direct observations of ultrasound microbubble contrast agent interaction with the microvessel wall. J Acoust Soc Am 2007;122:1191–200.

[45] Chen HKW, Brayman AA, Bailey MR, et al. Blood vessel deformations on microsecond time scales by ultrasonic cavitation. Phys Rev Lett 2011;106:034301.

[46] Sirsi SR, Borden BM. Advances in ultrasound mediated gene therapy using microbubble contrast agents. Theranostics 2012;2:1208–22.

[47] Brujan EANK, Schmidt P, Vogel A. Dynamics of laser-induced cavitation bubbles near elastic boundaries: influence of the elastic modulus. J Fluid Mech 2001;433:283–314.

[48] Liang CCY, Yi X, Xu J, et al. Nanoparticle-mediated internal radioisotope therapy to locally increase the tumor vasculature permeability for synergistically improved cancer therapies. Biomaterials 2019;197:368–79.

[49] Cherukuri PGE, Curley SA. Targeted hyperthermia using metal nanoparticles. Adv Drug Deliv Rev 2010;62:339–45.

[50] Theek BBM, Ojha T, Möckel D, et al. Sonoporation enhances liposome accumulation and penetration in tumors with low epr. J Control Release 2016;231:77–85.

[51] Liao JWX, Ran B, Peng J, et al. Polymer hybrid magnetic nanocapsules encapsulating ir820 and ptx for external magnetic field-guided tumor targeting and multifunctional theranostics. Nanoscale 2017;9:2479–91.

[52] Marano FAM, Frairia R, Adamini A, et al. Doxorubicin-loaded nanobubbles combined with extracorporeal shock waves: basis for a new drug delivery tool in anaplastic thyroid cancer. Thyroid 2016;26:706–16.

[53] Marano FFR, Rinella L, Argenziano M, et al. Combining doxorubicin-nanobubbles and shockwaves for anaplastic thyroid cancer treatment: preclinical study in a xenograft mouse model. Endocr Relat Cancer 2017;24:275–86.

[54] Varchi GFF, Canaparo R, Ballestri M, et al. Engineered porphyrin loaded core-shell nanoparticles for selective sonodynamic anticancer treatment. Nanomedicine 2015;10:3483–94.

[55] Canaparo RVG, Ballestri M, Foglietta F, et al. Polymeric nanoparticles enhance the sonodynamic activity of meso-tetrakis (4-sulfonatophenyl) porphyrin in an in vitro neuroblastoma model. Int J Nanomed 2013;8:4247–63.

[56] Dollet BMP, Garbin V. Bubble dynamics in soft and biological matter. Annu Rev Fluid Mech 2019;51:331–55.

[57] Ji QWP, He C. Extracorporeal shockwave therapy as a novel and potential treatment for degenerative cartilage and bone disease: osteoarthritis. A qualitative analysis of the literature. Prog Biophys Mol Biol 2016;121:255–65.

Chunyang Yin received her B.S. degree in Environmental Science from Shanxi University in 2012. Currently she is a Ph.D. student at the Research Center for Eco-Environmental Sciences, Chinese Academy of Sciences. Her research interest mainly focuses on modulating tumor microenvironment to reinforce the enhanced permeability and retention effect.

Yajun Liu is currently a chief physician of Orthopaedics at Beijing Jishuitan Hospital, China. He received his M.D. from the Health Science Center of Peking University in 2005. Thereafter, he works in Beijing Jishuitan Hospital as an orthopaedic surgeon. His research interests include (1) the basic and clinical studies on extracorporeal shock wave therapy; (2) the mechanisms regarding degeneration and repairment of bone and joints

Sijin Liu is currently a professor at the Research Center for Eco-Environmental Sciences, the Chinese Academy of Sciences. His research interests center on (1) the mechanisms responsible for environmental pollutant-mediated oncogenic effects; (2) nanotoxicity and translational toxicology.